

# Effects of driving signal waveshape on the velocity field and heat transfer of impinging synthetic jets

G. Paolillo<sup>1,\*</sup>, C.S. Greco<sup>1</sup>, T. Astarita<sup>1</sup>, G. Cardone<sup>1</sup>

1: Dept. of Industrial Engineering, University of Naples "Federico II", Napoli, Italy

\*Corresponding author: [gerardo.paolillo@unina.it](mailto:gerardo.paolillo@unina.it)

**Keywords:** Synthetic jets, Particle Image Velocimetry, Infrared Thermography

## ABSTRACT

The present work reports on the measurements of the velocity fields and the heat transfer of impinging synthetic jets driven by different waveshapes. The actuator consists of a loudspeaker oscillating inside a cavity provided with a circular nozzle. Sinusoidal input voltage signals with variable ejection duty cycle  $d$  (ratio of the duration of the positive part of the signal to the total period) are applied to investigate the influence of the waveshape on the jet dynamics and the thermal performance. A parametric study is carried by varying both  $d$  (0.3, 0.4, 0.5, 0.6, 0.7) and the Strouhal number  $St$  (0.062, 0.12, 0.19) at constant value of the Reynolds number (3,000) and fixed nozzle-to-plate distance (equal to 2 nozzle exit diameters). The phase and time-average evolution of the synthetic jets is characterized by means of planar Particle Image Velocimetry; simultaneous measurements of the heat transfer coefficients are carried out via infrared thermography using a heated thin foil as heat flux sensor. The present results show that  $d$  plays only a minor influence on the time-averaged velocity structure for all the values of the Strouhal number investigated. Nevertheless, for the highest value of  $St$  increasing  $d$  has a detrimental effect on the heat transfer. The phase-averaged velocity measurements reveal that this behaviour is essentially related to the reduced strength of the synthetic jet vortices formed during the ejection phase, which in fact dominate the heat transfer in such a configuration.

---

## 1. Introduction

Impinging jets are used in a wide variety of industrial processes that require rapid cooling or heating, from internal cooling of aircraft engine turbine blades and combustor injectors to drying of paper and ceramic, as well as electronics cooling (Carlomagno & Ianiro, 2014). In the class of impinging jets, synthetic jets have aroused particular interest from the heat and mass transfer community for their advantageous features, such as the high reliability, the simplicity of design and the reduced sizes of their actuators (even suitable for micro-metric applications) (Gallas et al., 2003; Chaudhari et al., 2009; Persoons, 2012; de Luca et al., 2014).

A synthetic jet is generated by the periodic oscillation of a wall (generally a diaphragm, a piezo-electric membrane or a piston) inside a cavity provided with an opening (generally an orifice or a

nozzle). The periodic variation of the cavity volume results in a periodic oscillation of the cavity pressure which in turn leads to alternate phases of ejection or suction of fluid across the opening. During the ejection phase, vortices form due to the flow separation at the exit of the orifice/nozzle, which then propagate downstream under their self-induced velocity. Therefore, a jet is “synthesized” from the ambient fluid without net mass flux across the opening.

The behaviour of a synthetic jet is essentially determined by two non-dimensional parameters: the Reynolds number  $Re = U_0 D / \nu$  and the Strouhal number  $St = f D / U_0$  where  $U_0$  is a characteristic velocity scale (generally related to the volume flow rate during the ejection phase),  $D$  is the exit section diameter,  $\nu$  the fluid kinematic viscosity and  $f$  the operating frequency. In impinging configurations, another relevant parameter is the dimensionless impingement distance  $H/D$ , with  $H$  being the exit section-to-plate distance. Several studies (Chaudhari et al., 2010; Persoons et al., 2011; Valiorgue et al., 2009; Greco et al., 2014, 2017, 2018) have investigated the effects of  $Re$ ,  $St$  and  $H/D$  on both the velocity field structure and the heat transfer capabilities of impinging synthetic jets and a quite extensive knowledge on this side has been gained.

In the present work, focus is given on a different point, specifically on the influence of the driving signal waveshape on the performance of impinging synthetic jets. Generally, a sinusoidal law of motion is imparted to the oscillating wall of the synthetic jet actuator, which results in sinusoidal pressure and exit velocity responses; in such a case, the Strouhal number is sufficient to characterize the behaviour of the jet (along with the other relevant parameters). However, when a different law of motion is assigned, a different evolution of the flow in the ejection and suction phases is expected, which can significantly change the overall jet structure and properties.

In the literature there are few works that have addressed such a problem; some studies (Herwig & Middelberg, 2008; Geng et al., 2015) have analysed the influence of triangular and rectangular waveshapes as alternatives to the sinusoidal one on the heat transfer capabilities of pulsed jets. Herwig & Middelberg (2008) investigated the effects of these three waveshapes and different combination of the same on both the thermal performance and the velocity field of impinging circular jets. At the same Strouhal number, they found that the rectangular waveshape outperforms all the remaining signals. Moreover, from their results it is evident that the triangular signal with linear increase and a subsequent negative step change leads to higher heat transfer rates than the specular signal, i.e., the triangular one with a positive step change and a subsequent linear decrease. Such a behaviour was also observed later by Geng et al. (2015), who argued that a sudden change of the jet velocity from a maximum to zero results in the destruction of the coherent vortex structures and development of unstructured turbulence which is beneficial to heat transfer. The results of Geng et al. (2015) are in agreement with those Herwig & Middelberg (2008), thus confirming that the rectangular waveshape is more effective than the sinusoidal and the triangular ones, while combinations of these signals leads to heat transfer enhancements intermediate between those of the individual signals.

An investigation similar to the above ones was carried out for synthetic jets in the numerical work of Y. Zhang et al. (2018). Sinusoidal, triangular and rectangular waveshapes were examined for

different values of the Strouhal number (0.012-2.4), the Reynolds number (1,533-7,776) and the dimensionless impingement distance (2-8), using the SST/ $k$ - $\omega$  turbulence model. Interestingly, it was shown that when  $St$  is around its optimal value, the triangular waveshape exhibits the best performance, while the rectangular one exhibits the worst one, whereas the latter can be better than the triangular and sinusoidal waveshapes only for small values of  $St$  ( $St < 0.06$ ). The very recent work of Singh et al. (2022), which explored the effects of the sinusoidal and square waveshapes on synthetic jets for  $Re$  in the range 1,656-2,218,  $H/D$  in the range 1-25 and  $St$  in the range 0.083-0.165, confirmed partially this result. In fact, it was observed that the average Nusselt number for the sinusoidal waveshape is 20.86% higher than that for the square one, although the latter leads to higher heat transfer in the stagnation region.

Canonical waveshapes, like the triangle and the rectangle, are not the only alternatives to sinusoids. A different approach consists in generating sinusoidal signals with varying suction duty cycle factor  $k$  (i.e., the duration of the suction phase in the synthetic jet operation cycle). The parameter  $k$  is defined as  $k = \tau_2/\tau_1$  with  $\tau_1$  and  $\tau_2$  being the durations of the phases of the periodic signal where it is positive or negative respectively. Based on numerical simulations, P. Zhang & Wang (2007) demonstrated that the suction duty cycle factor  $k$  affects the vortex strength of the vortices formed during the blowing phase, with practically no effect on their convection velocity and trajectory. Feng et al. (2010) and Feng & Wang (2012) analysed the effects of this parameter on the control of the separated flow around a circular cylinder, finding that by increasing  $k$  the flow separation is delayed and a drag reduction of up to 29% can be obtained. To the authors' knowledge, in the thermal management field no investigation on the effects of the sinusoidal waveshape with varying duty cycle has been carried out. For this reason, the present study reports on an investigation of the effects of the suction duty cycle factor on both the velocity fields and the heat transfer distributions of impinging synthetic jets. Particle Image Velocimetry (PIV) and Infrared Thermography (IR) are used to characterize the thermo-fluid dynamic behaviour of circular synthetic jets at fixed values of  $Re$  (3,000) and  $H/D$  (2) with varying  $St$  and  $k$ .

## 2. Experimental setup and techniques

### 2.1. Synthetic jet actuator and operating configurations

A schematic of the experimental apparatus is reported in Fig. 1. The synthetic jet actuator consists of a loudspeaker coupled with a cavity created inside a wooden box and provided with a nozzle on one side. The loudspeaker (CIARE HS250) has a free-space resonance frequency of 25 Hz, an external diameter of 270 mm, a nominal diameter of 208 mm and an equivalent oscillating mass of 56 g. The cavity has a volume of approximately  $2 \times 10^{-3} \text{ m}^3$ . The nozzle consists of a pipe with an inner diameter  $D$  of 21 mm and a length of  $9.5D$ . In all the present experiments, the nozzle exit section is positioned at a fixed distance from the impingement plate  $H = 2D$ .

The voltage input signal sent to the loudspeaker is generated by a signal generator (DIGILENT

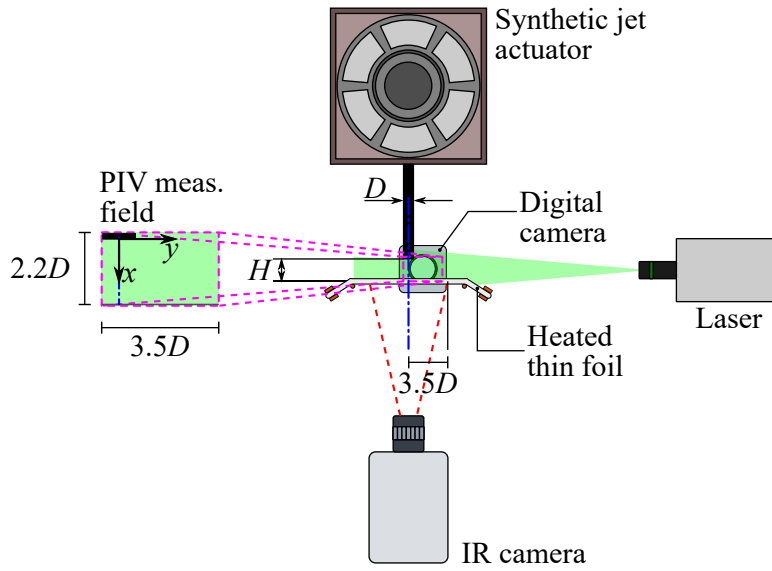


Figure 1. Schematic of the experimental apparatus.

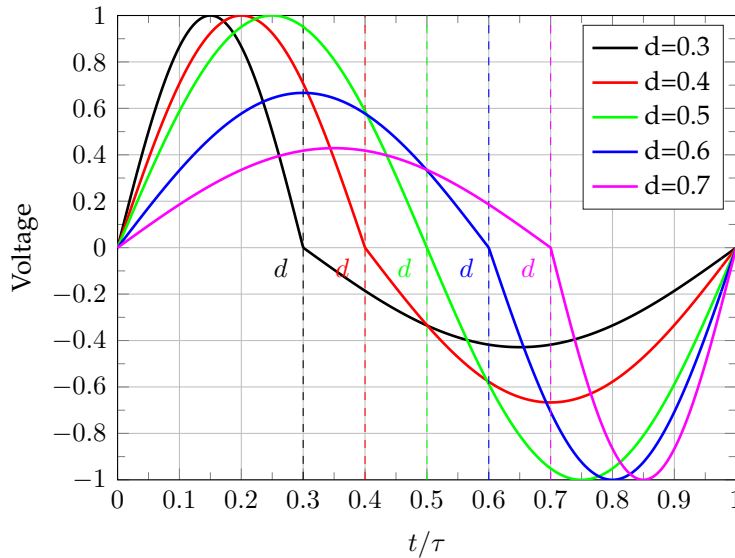


Figure 2. Sinusoidal driving input signal with varying the ejection duty cycle  $d$  at fixed unity amplitude.

Analog Discovery™) and amplified by a Hi-Fi amplifier (Kenwood KAC-6405). Sinusoidal waveshapes with different suction duty cycle factors are investigated in the current study. In the following, these waveshapes are identified by a different parameter, which is called the ejection duty cycle and denoted by  $d$ . The latter is defined as:  $d = \tau_1/\tau$  with  $\tau_1$  being the duration of the phase in which the signal is positive and  $\tau$  the period of the synthetic jet operation cycle. Since  $\tau = \tau_1 + \tau_2$  and  $k = \tau_2/\tau_1$ , the relationship between  $d$  and  $k$  is simply  $k = 1/d - 1$  (it is noticed that  $k$  varies between 0 and  $+\infty$ , whereas  $0 < d < 1$ ). Five different values of  $d$  are considered in the present investigation, namely  $d = 0.3, 0.4, 0.5, 0.6$  and  $0.7$ . Figure 2 shows the waveshapes corresponding to the latter case with fixed amplitude of the signal. The amplitude  $A$  of the sinusoidal waveshape

with varying  $d$  is defined as the maximum absolute value of the signal. Since the signal has zero mean, the amplitude  $A_1$  of the positive part of the signal ( $0 \leq t/\tau < d$ ) and the amplitude  $A_2$  of the negative part ( $d \leq t/\tau < 1$ ) are related to each other and, more specifically, the following relationship holds:  $dA_1 = (1 - d)A_2$ .

The parameter  $d$  is varied by keeping the Reynolds number fixed to the value  $Re = 3,000$ , which corresponds to a value of the characteristic velocity  $U_0$  of  $\approx 2.7$  m/s at the working temperatures of the experimental tests. The characteristic velocity is defined as the area- and time-averaged ejection velocity over the whole period of the operation cycle:

$$U_0 = \frac{2\pi}{\tau} \int_0^{\tau_1} \int_0^{D/2} \langle u_e \rangle(r, t) dr dt. \quad (1)$$

where  $\langle u_e \rangle$  is the azimuthally- and phase-averaged velocity profile of the jet at the exit section. In addition, three different values of the operating frequency  $f$ , i.e.,  $f = 8$  Hz, 16 Hz and 24 Hz, are investigated in order to evaluate the effect of the Strouhal number on the velocity and thermal fields of the impinging synthetic jets. The tested values of  $St$  are respectively 0.062, 0.12 and 0.19 (the corresponding values of the dimensionless stroke length  $L_0/D = 1/St$  are 16, 8 and 5.3).

For each pair of values of  $f$  and  $d$ , the selected value of the Reynolds number is reproduced by setting an appropriate value of the amplitude of the driving signal. This is performed iteratively based on preliminary PIV measurements.

## 2.2. PIV system

The PIV system consists of a low-speed double pulse Nd-YAG laser and a sCMOS camera (Andor Zyla with a resolution of 5.5 megapixels). The laser is shaped into a sheet with a thickness of approximately 1.5 mm, which illuminates the  $xy$ -plane containing a diameter of the circular nozzle. The flow is seeded by oil droplets with a nominal diameter of 1  $\mu\text{m}$  generated by a Laskin nozzle. The camera is arranged with its axis orthogonal to the laser sheet plane; it is provided with a 100 mm-focal length lens set at a relative aperture of 11. The spatial resolution is approximately 33 pixels/mm and the measurement region extends over  $2.2D$  diameter along the jet axis ( $x$ -direction) and  $3.5D$  in the crosswise direction, as shown in Fig. 1.

Phase-averaged measurements are performed by synchronizing the imaging system with the synthetic jet actuation. More specifically, the laser is operated at a frequency  $f_s$  lower than the operating frequency  $f$  of the synthetic jet and given by the following formula:

$$f_s = \frac{f}{\frac{1}{N_\varphi} + n} \quad (2)$$

where  $N_\varphi$  is the number of samples phases, equal to 30 in the present case, and  $n$  is an integer number. The sampling frequency  $f_s$  is thus set to a different value for each operating frequency of

the synthetic jet investigated in the current work. 200 samples for each phase are acquired, for a total of 6,000 snapshots.

The particle images are processed via an iterative image deformation algorithm using Blackman weighting windows; the final interrogation area size is  $64 \times 64$  pixels spaced by 8 pixels in both directions (vector pitch of 0.24 mm, i.e.,  $0.011D$ ). Further details about the PIV process can be found in Astarita & Cardone (2005) and Astarita (2006, 2007, 2008).

### 2.3. Infrared thermography system

The IR system consists essentially of a thermal camera and a heat flux sensor. The latter consists of a rectangular constantan foil with sizes  $262 \times 200$  mm and a thickness of  $50 \mu\text{m}$ . The foil is steadily and uniformly heated by Joule effect and cooled from the upper side by the synthetic air jet impinging on it. The Joule heating is obtained by applying a steady voltage difference to the edges of the foil by using a stabilized DC power supply. The lower side of the foil is coated by black paint with high emissivity ( $\varepsilon \approx 0.95$ ) and imaged by the thermal camera. In the present tests, a CEDIP JADE III camera with a resolution of  $320 \times 240$  pixels is used. The spatial resolution of the camera is 2.1 pixels/mm ( $\approx 44$  pixels/D) and the frame rate is 125 Hz for all the tests. Thus the thermal test covers only a first part of the velocimetry measurement test ( $\approx 1/8$  of the latter). Temperature variations across the foil thickness are negligible since the Biot number  $Bi$  is very small compared to unity ( $Bi = h_t s / \lambda_f$ , where  $h_t$  is the total heat transfer coefficient and  $s$  and  $\lambda_f$  are the foil thickness and thermal conductivity).

A local steady energy balance is applied to the foil to compute the convective heat transfer coefficients (Carlomagno & Cardone, 2010; Astarita & Carlomagno, 2012):

$$h(T_w - T_{aw}) = \dot{q}_j - \dot{q}_r - \dot{q}_k - \dot{q}_n \quad (3)$$

where:

- $h$  is the convective heat transfer coefficient;
- $T_w$  is the wall temperature measured via the IR camera;
- $T_{aw}$  is the adiabatic wall temperature. The latter is determined by means of specific tests (*cold tests*) during which the DC power supply is switched off and in fact the measured  $T_w$  coincides with  $T_{aw}$ ;
- $\dot{q}_j$  the Joule heat flux computed by measuring both the current and the voltage across the foil;
- $\dot{q}_r$  is the radiation heat loss evaluated as:  $\dot{q}_r = \varepsilon \sigma (T_w^4 - T_a^4)$  with  $\sigma$  being the Stefan-Boltzmann constant and  $T_a$  the ambient temperature. The latter is measured by means of a RTD sensor placed in the proximity of the impingement plate;

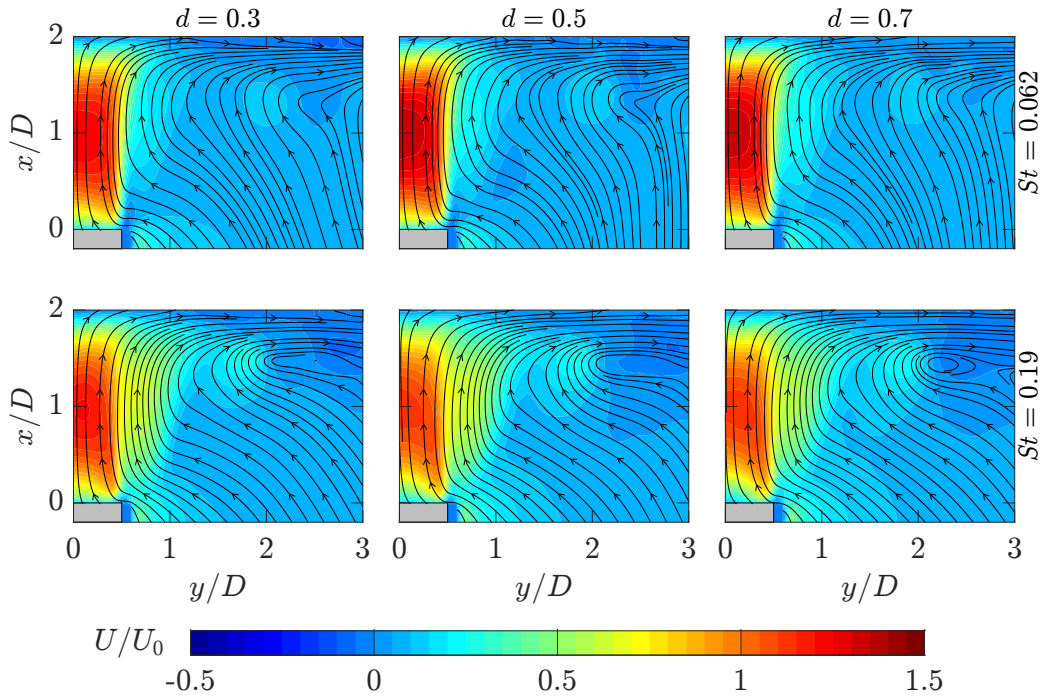


**Figure 3.** Time-averaged velocity fields with varying  $St$  and  $d$  for  $Re = 3,000$  and  $H/D = 2$ . Maps of the axial velocity with 2D streamlines superimposed.

- $\dot{q}_k = -\lambda_f s \nabla^2 T_w$  is the loss for tangential conduction;
- $\dot{q}_n$  is the loss for natural convection and is estimated via empirical correlations (Welty et al., 2009).

All the quantities in Eq. (3) are time-averaged and, in particular, their values are estimated by averaging over the whole duration of the thermal test. In the following, the heat transfer results are presented in terms of the Nusselt number:

$$Nu = hD/\lambda \tag{4}$$

where  $\lambda$  is the fluid thermal conductivity. Typical uncertainties for the present measurements of  $Nu$  are around 4% with a level of confidence of 95%.

### 3. Results

In the following, only the results for the lowest and the highest value of the Strouhal number investigated in the current study are presented and analysed. Figure 3 reports the time-averaged 2D velocity maps for these configurations and for values of the ejection duty cycle  $d$  equal to 0.3, 0.5 and 0.7; indeed, the middle column corresponds to the case of a purely sinusoidal waveshape ( $d = 0.5$ ). The figure shows that the variation of  $d$  has only secondary effects on the structure of the time-averaged velocity field. At  $St = 0.062$  the increase of  $d$  from 0.3 to 0.5 leads to an

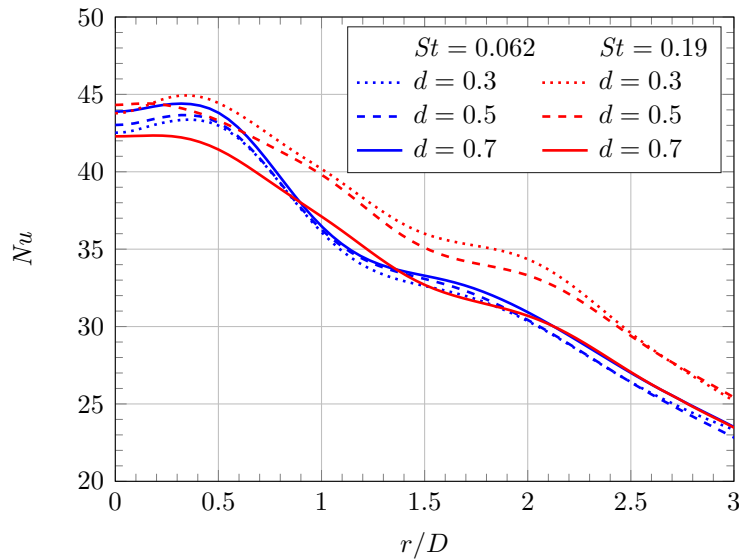


**Figure 4.** Azimuthally-averaged profile of the time-averaged Nusselt number with varying  $St$  and  $d$  for  $Re = 3,000$  and  $H/D = 2$ .

increase of the time-averaged axial velocities in the jet core around  $x/D = 1$ , whereas no significant difference is found between the cases corresponding to  $d = 0.5$  and  $d = 0.7$ . Conversely, at high  $St$ , the effect of varying the ejection duty cycle is essentially felt in the region in the proximity of the nozzle exit section, i.e., for  $x/D < 0.5$ . Here, the time-averaged axial velocities increase with decreasing  $d$ , which is a consequence of the higher velocity magnitudes of the jet in the ejection phase (characterized by a smaller duration at lower  $d$ ) and the lower velocity magnitudes in the subsequent suction phase. On the other side, from the comparison of the two rows in Fig. 3 it is evident that the increase of  $St$  results in an increase of the jet spreading rate and a subsequent reduction of the jet-core velocities. The latter behaviours are related to the higher strength of the synthetic jet vortices which cause more entrainment of the surrounding fluid and to the reduction of the trailing jet (column of the fluid following the synthetic jet primary vortex; e.g., see Greco et al. (2017)).

Figure 4 reports the radial profiles of the time-averaged Nusselt number for the same cases of Fig. 3. The variation of  $d$  has a minor effect even on heat transfer at the lowest value of  $St$  presented. In this case, a slight reduction of the Nusselt number values with decreasing the ejection duty cycle is found, whereas the shape of the heat transfer distribution keeps essentially unchanged. At the highest value of  $St$ , the waveshapes with  $d = 0.3$  and  $d = 0.5$  exhibit a similar trend, with the former configuration outperforming the latter one; interestingly, the case with  $d = 0.3$  presents a local peak of  $Nu$  at  $r/D \approx 0.35$ , while in the case with  $d = 0.5$  a plateau is observed around the impingement center. By increasing  $d$  from 0.5 to 0.7 a substantial reduction of the  $Nu$  values occurs; this causes the synthetic jet to produce heat transfer rates comparable to those of the configurations with  $St = 0.062$  at least for  $r/D > 0.9$ . Conversely, for  $d \leq 0.5$  the configurations with higher  $St$  offer better heat transfer outside of the stagnation region ( $r/D > 0.5$ ).

In order to better understand the above behaviours, the phase-average evolution of the synthetic

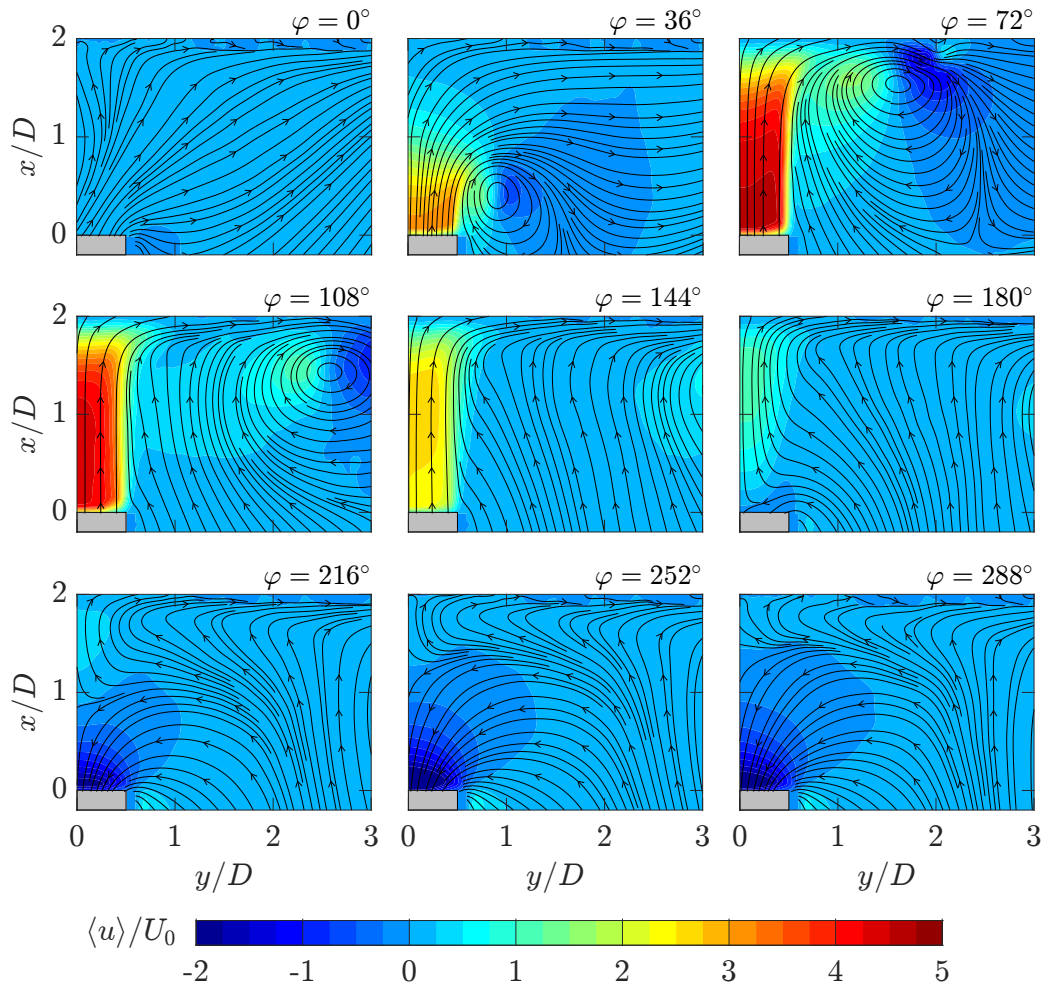


**Figure 5.** Evolution of the phase-averaged velocity field for  $St = 0.062$ ,  $d = 0.5$ ,  $Re = 3,000$  and  $H/D = 2$ . Maps of the axial velocity with 2D streamlines superimposed.

jets is analysed in the following. For  $St = 0.062$  only the case corresponding to  $d = 0.5$  is presented, since no significant differences are observed with respect to the other waveshapes. Nine different phases with a spacing of  $36^\circ$  are reported in Fig. 5. The phase  $\varphi = 0^\circ$  corresponds to the beginning of the ejection phase of the operation cycle and among the sampled phases it is identified as the one in which the phase-averaged velocity  $\langle u \rangle$  at the point  $(x, y) = (0, 0)$  switches from a negative to a positive value. The evolution of this synthetic jet is characterized by the formation of a large scale vortex (first visible in  $\varphi = 36^\circ$ ) which propagates along the wall and suddenly disappears from the field of view (the vortex center is already outside the measurement region at  $\varphi = 144^\circ$ ). After the formation of the vortex, the fluid ejection results in the development of a trailing jet which impinges the wall as a conventional round jet. At the beginning of the suction phase ( $\varphi = 180^\circ$ ), the vortex is far from the jet axis, while the velocities in trailing jet core are small compared to the maximum values attained in the ejection phase, although higher in magnitude than those found at  $\varphi = 0^\circ$ . In the second half of the cycle the extent of the suction field is delimited by a saddle point, which moves from the exit section to approximately  $0.5D$  from the wall (location reached at  $\varphi = 288^\circ$ ).

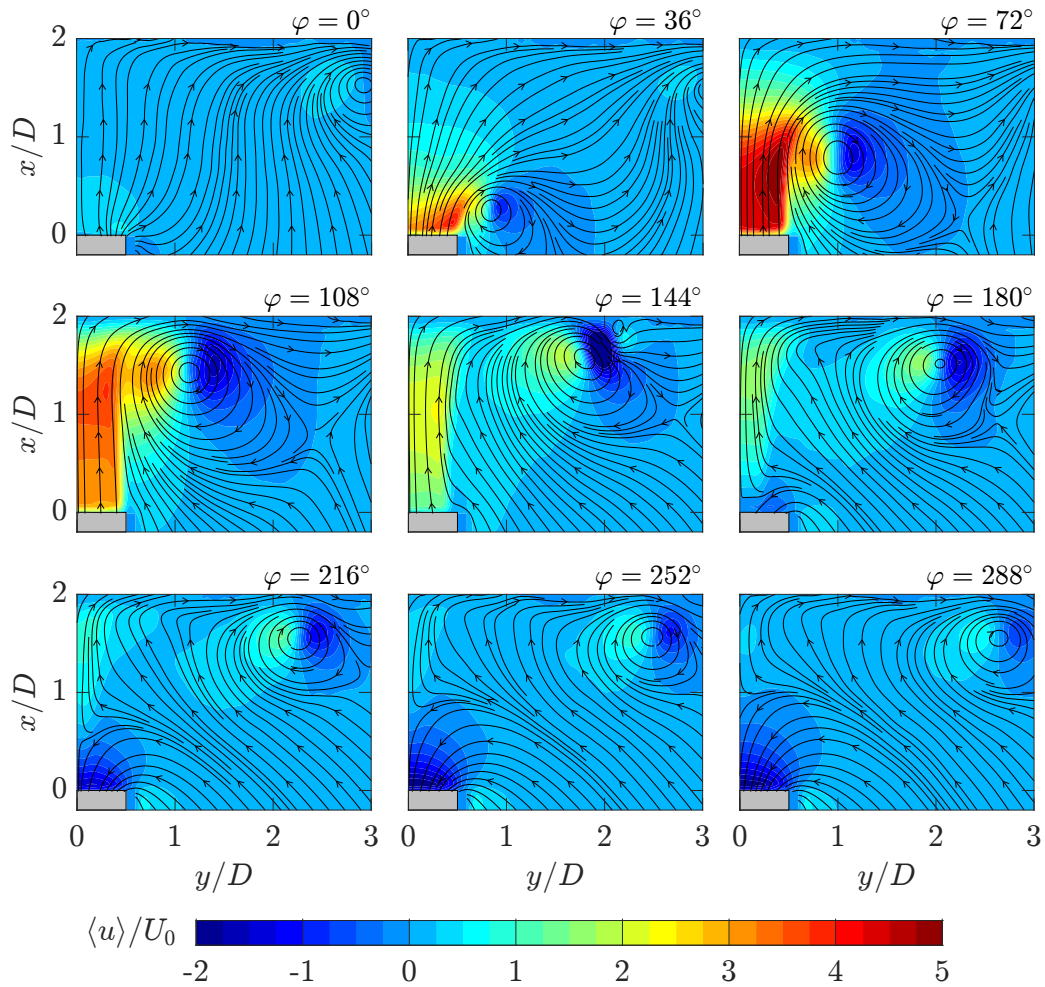


**Figure 6.** Evolution of the phase-averaged velocity field for  $St = 0.19$ ,  $d = 0.3$ ,  $Re = 3,000$  and  $H/D = 2$ . Maps of the axial velocity with 2D streamlines superimposed.

The evolution at higher  $St$  is shown in Fig. 6 for  $d = 0.3$  and Fig. 7 for  $d = 0.7$ . In these cases, the vortex formed in one period is still detectable at the beginning of the following operation cycle; in particular, at  $\varphi = 0^\circ$ , the vortex center is detected near the boundary of the present measurement region (i.e.,  $y/D = 3$ ) for both the configurations displayed in Fig. 6 and Fig. 7. This is a consequence of the higher operating frequency, rather than the reduced flow velocities, which are comparable to those at lower  $St$ . A remarkable difference from the latter case is the reduced size of the synthetic jet vortex: while for  $St = 0.062$  the vortex diameter is approximately  $2D$ , for  $St = 0.19$  it is only  $1D$ . Such a reduced size comes with a greater strength of the vortex. In particular, for  $d = 0.3$  (Fig. 6) it is possible to notice high negative axial velocities (directed away from the wall) in front of the propagating vortex at  $\varphi = 144^\circ$ , which induce a local flow separation and the formation of recirculation region near the wall. The vortex induction remains significantly large also in the subsequent propagation during the suction phase ( $180^\circ < \varphi < 360^\circ$ ); indeed, it is this induction that limits the displacement of the synthetic jet saddle point with respect to the case with lower  $St$  (Fig. 5). The greater vortex strength in this configuration explains the higher values of  $Nu$ , while the formation of separated regions on the wall results in inflection points in the radial

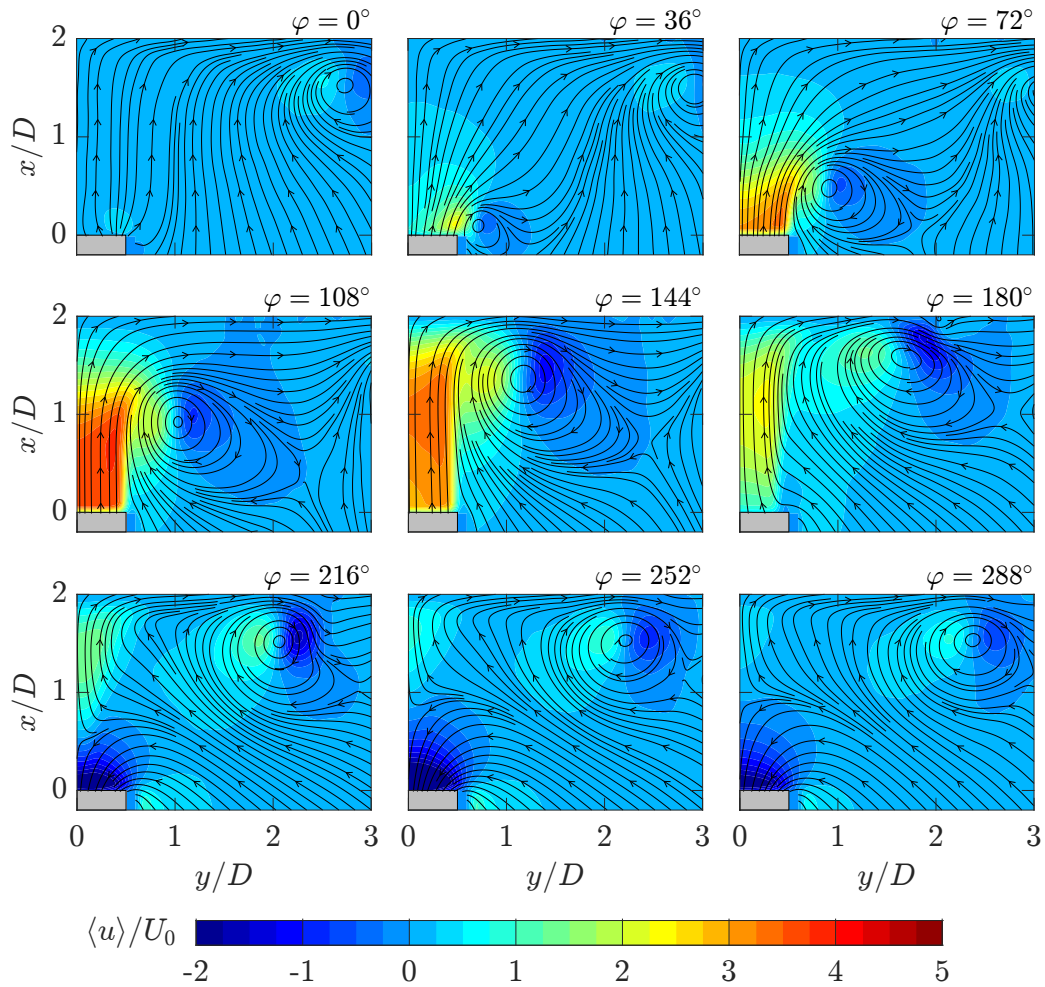


**Figure 7.** Evolution of the phase-averaged velocity field for  $St = 0.19$ ,  $d = 0.7$ ,  $Re = 3,000$  and  $H/D = 2$ . Maps of the axial velocity with 2D streamlines superimposed.

profile of the time-averaged Nusselt number (Fig. 4).

The evolution for the synthetic jet driven by the waveform with  $d = 0.7$  is similar to that for  $d = 0.3$ ; nevertheless, the strength of the vortex is significantly smaller. This is evident from the lowered velocities induced by the vortex itself since the very beginning of its formation ( $\varphi = 36^\circ$ ). For instance, it is noticed that for  $d = 0.3$  while the jet emerges from the exit nozzle ( $\varphi = 72^\circ$  and  $\varphi = 108^\circ$ ) the forming vortex produces a region of positive axial velocities at the jet periphery (localized at  $y/D \approx 0.5$ ) that are the same magnitude as the velocities in the core. Conversely, in the  $d = 0.5$  case the velocities in such a region are comparable those in the front part of the jet column. Also during the following propagation along the wall, the vortex induces smaller negative axial velocities in its forehead region, which result in a reduced extent of the separation zone. The smaller vortex strength for  $d = 0.7$  is ascribable to the smaller flow accelerations that characterize the ejection phase of this synthetic jet and is accompanied by a reduced vortex propagation velocity, as visible from comparison of the maps in Fig. 6 and Fig. 7. Ultimately, it is possible to conclude that the drop of the Nusselt numbers observed at high Strouhal number when increasing the ejection duty cycle is mainly related to the reduction of the intensity of the synthetic jet vortices, which in fact

dominate the heat transfer in this configuration.

#### 4. Conclusions

This work has focused on the characterization of the velocity fields and the thermal performances of impinging synthetic jets driven by different waveshapes. Specifically, sinusoidal driving signals with variable ejection duty cycle  $d$  have been investigated for different values of the Strouhal number  $St$  (0.062, 0.12 and 0.19) and fixed values of  $Re$  (equal to 3,000) and  $H/D$  (equal to 2). PIV is used to visualize the impinging velocity field in one azimuthal plane containing the diameter of the circular exit section, whereas IR thermography is applied to measure the distribution of the convective heat transfer coefficients over the wall using a heated thin foil as heat flux sensor.

The present results show that the variation of  $d$  has relevant effects on both the flow field evolution and the heat transfer only at sufficiently high Strouhal numbers. At the lowest value of  $St$  investigated a moderate increase in the Nusselt numbers is found when increasing  $d$ ; at the highest value of  $St$ , the opposite trend is observed and by increasing  $d$  from 0.3 to 0.7 a drop of  $Nu$  values up to 5% in the region  $r/D < 0.5$  occurs. The latter behaviour is essentially associated with the reduced strength of the synthetic jet vortices, which play a key role in the impingement heat transfer at high values of  $St$ .

#### Nomenclature

##### *Roman letters*

$A$	Amplitude of the input signal [V]
$A_1$	Amplitude of the positive part of the input signal [V]
$A_2$	Amplitude of the negative part of the input signal [V]
$Bi$	Biot number
$d$	Ejection duty cycle
$D$	Nozzle exit section [m]
$f$	Actuation frequency [Hz]
$f_s$	PIV sampling frequency [Hz]
$h$	Convective heat transfer coefficient [ $\text{W m}^{-2} \text{K}^{-1}$ ]
$H$	Nozzle-to-plate distance [m]
$h_t$	Total heat transfer coefficient [ $\text{W m}^{-2} \text{K}^{-1}$ ]
$k$	Suction duty cycle factor
$L_0$	Stroke length [m]
$n$	Integer number of periods
$N_\varphi$	Number of sampled phases
$Nu$	Nusselt number
$\dot{q}_j$	Joule heat flux [ $\text{W m}^{-2}$ ]

$\dot{q}_k$	Tangential conduction heat flux [ $\text{W m}^{-2}$ ]
$\dot{q}_n$	Natural convection heat flux [ $\text{W m}^{-2}$ ]
$\dot{q}_r$	Radiation heat flux [ $\text{W m}^{-2}$ ]
$r$	Radial coordinate [m]
$Re$	Reynolds number
$s$	Foil thickness [m]
$St$	Strouhal number
$t$	Time instant [s]
$T_a$	Ambient temperature [K]
$T_{aw}$	Adiabatic wall temperature [K]
$T_w$	Wall temperature [K]
$\langle u \rangle$	Phase-averaged velocity [m/s]
$\langle u_e \rangle$	Azimuthally- and phase-averaged exit velocity [m/s]
$U$	Time-averaged velocity [m/s]
$U_0$	Synthetic jet characteristic velocity [ $\text{m s}^{-1}$ ]
$x, y$	Spatial coordinates [m]

### **Greek letters**

$\varepsilon$	Paint emissivity
$\lambda_f$	Fluid thermal conductivity [ $\text{W m}^{-1} \text{K}^{-1}$ ]
$\lambda_f$	Foil thermal conductivity [ $\text{W m}^{-1} \text{K}^{-1}$ ]
$\nu$	Fluid kinematic viscosity [ $\text{m}^2 \text{s}^{-1}$ ]
$\sigma$	Stefan-Boltzmann constant [ $\text{kg s}^{-3} \text{K}^{-4}$ ]
$\tau$	Actuation period [s]
$\tau_1$	Duration of the positive part of the input signal [s]
$\tau_2$	Duration of the negative part of the input signal [s]
$\varphi$	Phase angle [deg]

### **References**

- Astarita, T. (2006). Analysis of interpolation schemes for image deformation methods in PIV: effect of noise on the accuracy and spatial resolution. *Experiments in Fluids*, 40(6), 977–987.
- Astarita, T. (2007). Analysis of weighting windows for image deformation methods in PIV. *Experiments in Fluids*, 43(6), 859–872.
- Astarita, T. (2008). Analysis of velocity interpolation schemes for image deformation methods in PIV. *Experiments in Fluids*, 45(2), 257–266.

- Astarita, T., & Cardone, G. (2005). Analysis of interpolation schemes for image deformation methods in PIV. *Experiments in Fluids*, 38(2), 233–243.
- Astarita, T., & Carlomagno, G. M. (2012). *Infrared thermography for thermo-fluid-dynamics*. Springer-Verlag Berlin Heidelberg: Springer Science & Business Media.
- Carlomagno, G. M., & Cardone, G. (2010). Infrared thermography for convective heat transfer measurements. *Experiments in Fluids*, 49(6), 1187–1218.
- Carlomagno, G. M., & Ianiro, A. (2014). Thermo-fluid-dynamics of submerged jets impinging at short nozzle-to-plate distance: a review. *Experimental Thermal and Fluid Science*, 58, 15–35.
- Chaudhari, M., Puranik, B., & Agrawal, A. (2010). Heat transfer characteristics of synthetic jet impingement cooling. *International Journal of Heat and Mass Transfer*, 53(5-6), 1057–1069.
- Chaudhari, M., Verma, G., Puranik, B., & Agrawal, A. (2009). Frequency response of a synthetic jet cavity. *Experimental Thermal and Fluid Science*, 33(3), 439–448.
- de Luca, L., Girfoglio, M., & Coppola, G. (2014). Modeling and experimental validation of the frequency response of synthetic jet actuators. *AIAA Journal*, 52(8), 1733–1748.
- Feng, L.-H., & Wang, J.-J. (2012). Synthetic jet control of separation in the flow over a circular cylinder. *Experiments in Fluids*, 53(2), 467–480.
- Feng, L. H., Wang, J. J., & Pan, C. (2010). Effect of novel synthetic jet on wake vortex shedding modes of a circular cylinder. *Journal of Fluids and Structures*, 26(6), 900–917.
- Gallas, Q., Holman, R., Nishida, T., Carroll, B., Sheplak, M., & Cattafesta, L. (2003). Lumped element modeling of piezoelectric-driven synthetic jet actuators. *AIAA Journal*, 41(2), 240–247.
- Geng, L., Zheng, C., & Zhou, J. (2015). Heat transfer characteristics of impinging jets: The influence of unsteadiness with different waveforms. *International Communications in Heat and Mass Transfer*, 66, 105–113.
- Greco, C. S., Cardone, G., & Soria, J. (2017). On the behaviour of impinging zero-net-mass-flux jets. *Journal of Fluid Mechanics*, 810, 25–59.
- Greco, C. S., Ianiro, A., & Cardone, G. (2014). Time and phase average heat transfer in single and twin circular synthetic impinging air jets. *International Journal of Heat and Mass Transfer*, 73, 776–788.
- Greco, C. S., Paolillo, G., Ianiro, A., Cardone, G., & De Luca, L. (2018). Effects of the stroke length and nozzle-to-plate distance on synthetic jet impingement heat transfer. *International Journal of Heat and Mass Transfer*, 117, 1019–1031.

- Herwig, H., & Middelberg, G. (2008). The physics of unsteady jet impingement and its heat transfer performance. *Acta Mechanica*, 201(1), 171–184.
- Persoons, T. (2012). General reduced-order model to design and operate synthetic jet actuators. *AIAA Journal*, 50(4), 916–927.
- Persoons, T., McGuinn, A., & Murray, D. B. (2011). A general correlation for the stagnation point Nusselt number of an axisymmetric impinging synthetic jet. *International Journal of Heat and Mass Transfer*, 54(17-18), 3900–3908.
- Singh, P. K., Renganathan, M., Yadav, H., Sahu, S. K., Upadhyay, P. K., & Agrawal, A. (2022). An experimental investigation of the flow-field and thermal characteristics of synthetic jet impingement with different waveforms. *International Journal of Heat and Mass Transfer*, 187, 122534.
- Valiorgue, P., Persoons, T., McGuinn, A., & Murray, D. (2009). Heat transfer mechanisms in an impinging synthetic jet for a small jet-to-surface spacing. *Experimental Thermal and Fluid Science*, 33(4), 597–603.
- Welty, J. R., Wicks, C. E., Rorrer, G., & Wilson, R. E. (2009). *Fundamentals of momentum, heat, and mass transfer* (Fifth ed.). John Wiley & Sons.
- Zhang, P., & Wang, J. (2007). Novel signal wave pattern for efficient synthetic jet generation. *AIAA Journal*, 45(5), 1058–1065.
- Zhang, Y., Li, P., & Xie, Y. (2018). Numerical investigation of heat transfer characteristics of impinging synthetic jets with different waveforms. *International Journal of Heat and Mass Transfer*, 125, 1017–1027.